ARTICLES

Controllable growth of wafer-scale PdS and PdS$_2$ nanofilms via chemical vapor deposition combined with an electron beam evaporation technique

Hui Gao[1, ‡], Hongyi Zhou[1, ‡], Yulong Hao[2, ‡], Guoliang Zhou[3], Huan Zhou[1], Fenglin Gao[1], Jinbiao Xiao[1], Pinghua Tang[1], and Guolin Hao[1, 4, †]

[1]School of Physics and Optoelectronics and Hunan Institute of Advanced Sensing and Information Technology, Xiangtan University, Xiangtan 411105, China

[2]College of Physics and Technology & Guangxi Key Laboratory of Nuclear Physics and Technology, Guangxi Normal University, Guilin 541004, China

[3]Department of Electronic and Electrical Engineering, University of Sheffield, Sheffield S10 2TN, UK

[4]National Laboratory of Solid State Microstructures, Nanjing University, Nanjing 210093, China

Abstract: Palladium (Pd)-based sulfides have triggered extensive interest due to their unique properties and potential applications in the fields of electronics and optoelectronics. However, the synthesis of large-scale uniform PdS and PdS$_2$ nanofilms (NFs) remains an enormous challenge. In this work, 2-inch wafer-scale PdS and PdS$_2$ NFs with excellent stability can be controllably prepared via chemical vapor deposition combined with electron beam evaporation technique. The thickness of the pre-deposited Pd film and the sulfurization temperature are critical for the precise synthesis of PdS and PdS$_2$ NFs. A corresponding growth mechanism has been proposed based on our experimental results and Gibbs free energy calculations. The electrical transport properties of PdS and PdS$_2$ NFs were explored by conductive atomic force microscopy. Our findings have achieved the controllable growth of PdS and PdS$_2$ NFs, which may provide a pathway to facilitate PdS and PdS$_2$ based applications for next-generation high performance optoelectronic devices.

Key words: PdS; PdS$_2$; nanofilms; controllable growth; chemical vapor deposition; electron beam evaporation

1. Introduction

Since the discovery of graphene in 2004, two-dimensional (2D) materials have attracted intensive attention due to their intriguing properties[1–4]. Recently, group-10 novel TMDs (nTMDs) have received a lot of attention because of their attractive properties including widely-tunable bandgap, high carrier mobility, anisotropy, and long-term air stability[5–9]. PdS$_2$, as a typical member of the nTMDs family, exhibits a unique pentagonal-layered structure and tunable bandgap (indirect band gap in monolayer and semi-metallic in bulk), which has created much interest in electronic, optoelectronic and anisotropic applications[10–14]. Moreover, 2D PdS$_2$ nanostructures display broad application prospects in the fields of thermoelectricity, piezoelectricity, nonlinear optics, and catalysis[15–17]. At present, PdS$_2$ nanoflakes are mainly prepared by liquid-phase exfoliation or chemical vapor transport methods[10, 18]. Nevertheless, these methods have the limitation of uncontrollable sample size and thickness, and inevitably introduce impurities during the synthe-

sis process, which cannot meet the requirements of practical applications. Therefore, it is crucial to develop an effective approach to synthesize high-quality and large-scale 2D PdS$_2$ nanofilm (NF) for fundamental research and future application. Direct sulfurization/selenization of pre-deposited metals or oxides has been demonstrated to be an effective method for preparing large-area films[19–21].

PdS is a typical nonlayered semiconducting material with a tetragonal structure, which has also attracted considerable attention due to its intriguing properties in the last few decades[22–25]. PdS has been demonstrated to be n-type semiconductor with high carrier density ($(8.0 \pm 2.0) \times 10^{18}$ cm^{-3}) and electron mobility ((20 ± 2) cm^2/(V·s))[22]. Moreover, PdS exhibits high optical absorption coefficient (higher than 10^5 cm^{-1} at photon energies $hv > 2.0$ eV) and ideal band gap energy (~1.6 eV), which make it an appealing material for potential applications in photoelectrochemical energy conversion, thermoelectricity and solar cells[22–27]. Extensive efforts have been made to investigate the precise growth of PdS and PdS$_2$ nanostructures. However, the controllable synthesis of PdS and PdS$_2$ NFs still faces significant challenges.

In this work, we have achieved the precise growth of 2 inch wafer-scale uniform PdS and PdS$_2$ NFs via chemical vapor deposition (CVD) combined with electron beam evaporation (EBE) technique. Our experimental results demonstrate that the thickness of pre-deposited Pd and sulfurization tem-
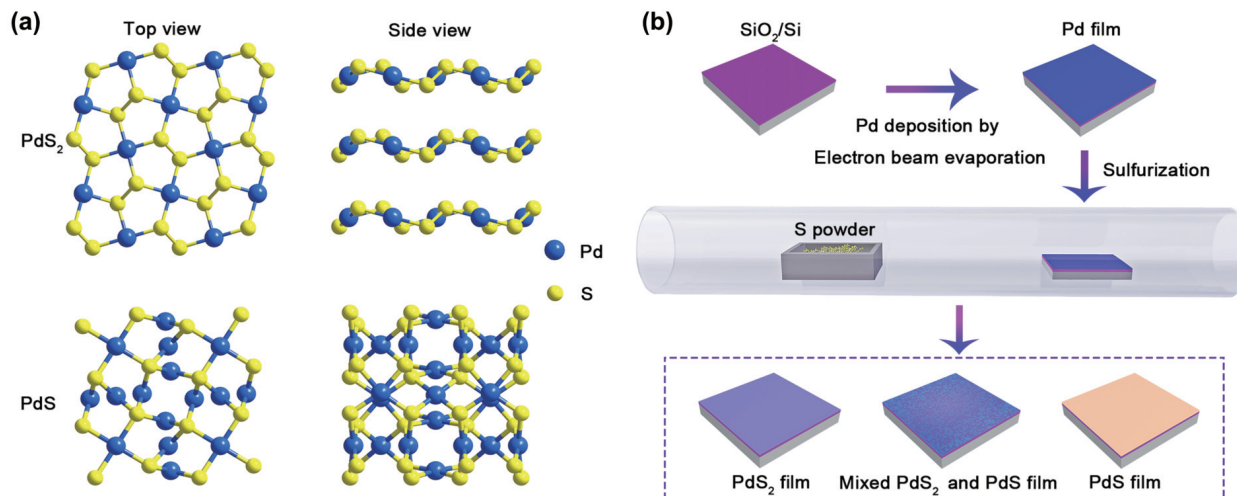
Fig. 1. (Color online) (a) Side and top views of the schematic crystal structures for PdS_2 and PdS. (b) Schematic for the synthesis of PdS and PdS_2 NFs.

perature are critical for the controllable synthesis of PdS and PdS_2 NFs. The corresponding growth mechanism was further proposed based on our experimental results and Gibbs free energy calculations. In addition, the PdS_2-based thin film field-effect transistors (TFTs) were investigated exhibiting n-type behavior. Our study provides a facile strategy for fabricating wafer-scale uniform PdS and PdS_2 NFs, which can be a guidance for the synthesis of other 2D material systems.

2. Experimental details

Pd NFs with different thicknesses were deposited on the SiO_2/Si substrate by employing the electron-beam evaporation method (EBE, DE400DHL). The as-deposited Pd films were placed at the center zone of the growth furnace while sulfur (S) powder (1 g, 99.9%, Aladdin) was located at the upstream zone. The quartz tube was purged for 20 min with 500 standard cubic centimeters per minute (sccm) Ar gas to remove residue air. Then the Ar flow rate was reduced to 50 sccm during the growth process. The temperature of the center zone was heated to 500 °C for 25 min and kept under this temperature for 10 min.

The morphologies and nanostructures of as-prepared samples were carried out by optical microscopy (OM, Nikon, LV150N) and atomic force microscopy (AFM, Bruker Dimension Icon). The surface potential distribution and local electrical properties were systematically performed by Kelvin probe force microscopy (KPFM) and conductive AFM (C-AFM, Bruker Dimension Icon). The KPFM and C-AFM measurements were conducted in an ambient environment and the humidity was around 30%. Raman spectra and mappings of the as-prepared sample were investigated by a Raman spectrometer (Witec Alpha 300R) with a 532 nm laser excitation. The composition and chemical bonding states of as-synthesized sample were examined by X-ray photoelectron spectroscopy (XPS, Thermo Scientific K-Alpha). The crystallographic structure and the quality of as-prepared samples were characterized by transmission electron microscopy (TEM), high-resolution TEM (HRTEM), selected area electron diffraction (SAED) and energy dispersive spectroscopy (EDS; JEOL 2100F).

The back-gated TFT based on PdS_2 NF was fabricated by laser direct writing lithography (Microwriter ML Baby), reac-

tive ion etching (Haasrode-R200A), and EBE (DE400DHL). First, the source (S) and drain (D) regions were defined by photolithography, and a Ti/Pd/Au (0.6 nm thick Ti, 20 nm thick Pd and 30 nm thick Au) film was deposited by EBE. Second, redundant PdS_2 were etched by photolithography and the reactive ion etching (RIE) process under oxygen plasma for 60 s. As-prepared devices were measured using a semiconductor analysis system (Keithley 4200A-SCS).

3. Results and discussions

A the schematic top view and side view crystal structures of PdS_2 and PdS are shown in Fig. 1(a). In 2O phase PdS_2, two Pd atoms and three S atoms form a wrinkled pentagonal ring and each Pd atom combines with four S atoms in the same plane while a covalent S–S bond is formed between two neighboring S atoms[7]. The crystal structure of PdS is the tetragonal structure, which belongs to the space group of P42/m (84). Fig. 1(b) presents the schematic diagram of the growth setup for synthesizing PdS and PdS_2 NFs. Figs. S1(a) and S1(b) show the AFM images before and after the sulfurization when the pre-deposited Pd film thickness is 0.5 nm. Raman spectra (Fig. S1(c)) confirmed that the products are not PdS_2 or PdS under different sulfurization temperatures. Interestingly, pure PdS_2 NF can be synthesized when the thickness of pre-deposited Pd film is increased to 1 nm. A typical OM image of the PdS_2 is shown in Fig. 2(a), and the inset exhibits the corresponding photo image of as-prepared 2-inch PdS_2 NF grown on SiO_2/Si substrates. Fig. 2(b) presents Raman spectrum of the synthesized PdS_2 NF. Two Raman peaks were observed at 299 cm^{-1} and 422 cm^{-1} corresponding to the E_g mode and A_g mode of PdS_2, respectively, which are in good agreement with previous reports[13]. Raman mapping of the representative A_g mode (422 cm^{-1}) is displayed in Fig. 2(c), which indicates the uniformity of as-grown PdS_2 NF. The inset shows corresponding OM image. We found that Raman spectra exhibit clear characteristic peaks with unchanged Raman signals when the sample was stored in air for six months (Fig. S2), which means that the as-prepared PdS_2 NF exhibits excellent air stability. Fig. 2(d) shows the representative AFM image of PdS_2 NF. The surface potential of as-synthesized PdS_2 NF was investigated by KPFM (Fig. 2(e)).
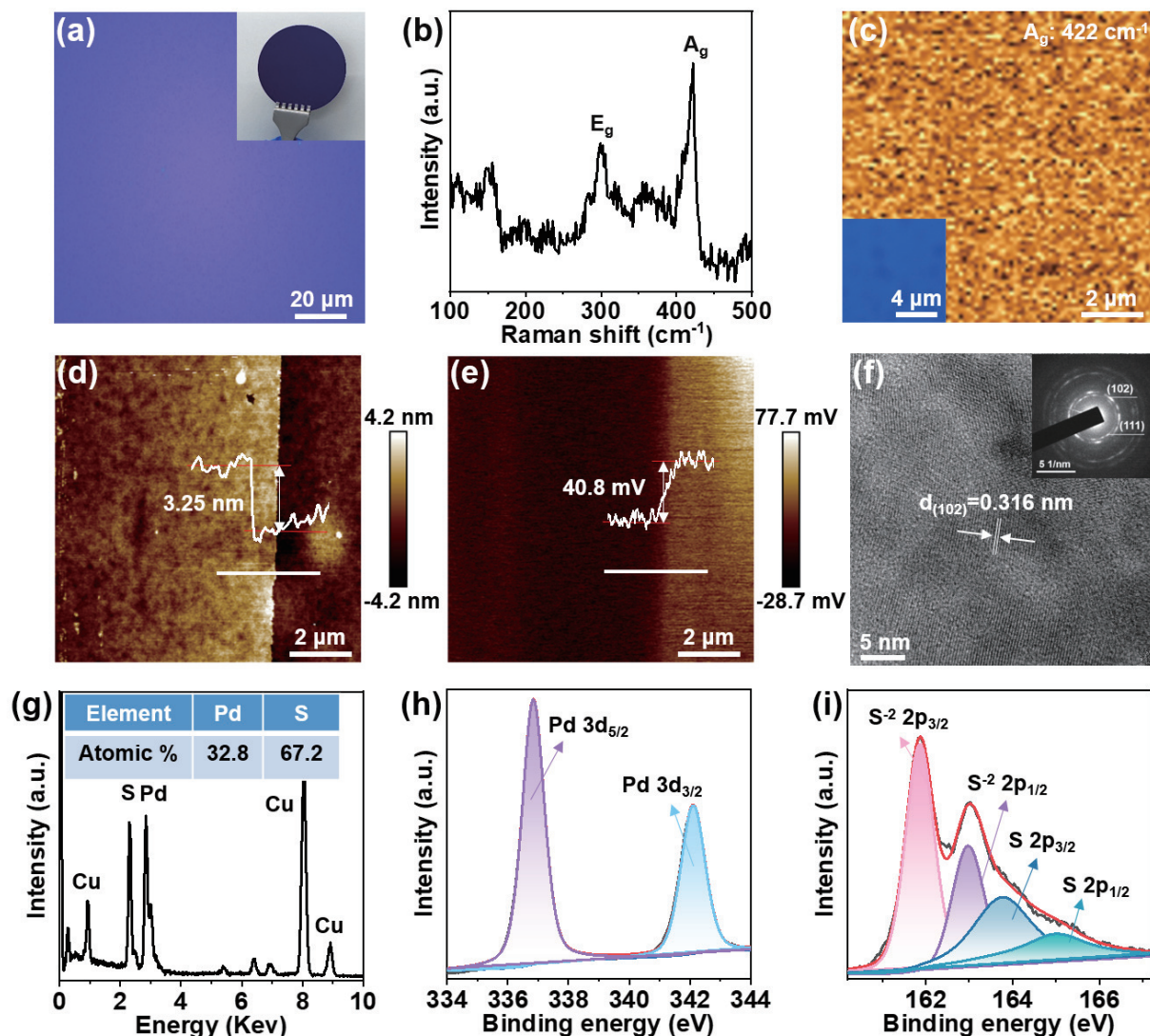
Fig. 2. (Color online) (a) OM image of as-prepared PdS_2 NF (the thickness of pre-deposited Pd ~1 nm). Inset: photograph of 2-inch wafer-scale PdS_2 NF. (b) Raman spectrum of as-prepared PdS_2 NF. (c) Raman intensity mapping (A_g mode) of PdS_2 NF. Inset: corresponding OM image. (d) AFM image of PdS_2 NF. (e) Corresponding surface potential image. (f) HRTEM image of PdS_2 NF. Inset: corresponding SAED pattern. (g) EDS analysis of PdS_2 NF. (h, i) XPS spectra of the PdS_2 NF corresponding to Pd $3d$ and S $2p$ core level peaks, respectively.

The as-prepared PdS_2 NF displays a homogeneous surface potential distribution, which means that the as-prepared films are uniform. In addition, it is beneficial to fabricate PdS_2-based optoelectronic devices with relatively consistent performance.

To investigate the crystalline nature and chemical composition of as-synthesized PdS_2 NF, HRTEM, SAED and EDS characterizations were systematically performed. The HRTEM image presents clear lattice fringes indicating high-quality crystallinity of PdS_2 as shown in Fig. 2(f). The lattice distance is found to be 0.316 nm corresponding to the (102) plane of PdS_2. The inset is the corresponding SAED pattern, which shows two ring shapes corresponding to the PdS_2 planes of (111) and (102), respectively. SAED pattern indicates that the PdS_2 NF is polycrystalline. The EDS spectrum confirms that the atomic ratio between S and Pd elements is determined to be 1.95 : 1 as shown in Fig. 2(g). To further explore the composition and element bonding states, XPS was conducted for the as-prepared PdS_2 NF. The high-resolution XPS spectra of Pd $3d$ and S $2p$ of the synthesized PdS_2 are presented in Figs. 2(h) and 2(i), respectively. Two peaks at 336.86 eV

(Pd $3d_{5/2}$) and 342.08 eV (Pd $3d_{3/2}$) have been detected, which are ascribed to the S–Pd bonding of PdS_2[28]. The S $2p$ regions for PdS_2 NF are fitted with two doublets from two chemical states of sulfur. The two peaks at 161.78 and 162.88 eV can be ascribed to the S–Pd bonding state of PdS_2, respectively. Meanwhile, elemental sulfur was detected at 163.76 and 165.01 eV, corresponding to the S $2p_{3/2}$ and S $2p_{1/2}$, respectively[29]. To investigate the influence of sulfurization time on the synthesis of PdS_2 NF, we have fabricated PdS_2 NFs under different sulfurization time. Figs. S3(a)–S3(e) present AFM images of as-prepared samples with sulfurization time to be 10, 30, 60, 120, and 180 min, respectively. It is clear that the thickness was maintained at ~3.3 nm as displayed in Fig. S3(f). When the sulfurization time was 10 min, the root-mean-square roughness (Rq) was 0.46 nm. And when the sulfurization time was extended to 30 min or much longer, the Rq was around 1.8 nm (Fig. S3(g)). Fig. S3(h) displays the corresponding Raman spectra. Fig. S3(i) shows the position evolution of A_g and E_g modes as a function of sulfurization time. No variation in Raman peak positions of PdS_2 NFs was observed, which confirmed the PdS_2 NF can be suc-
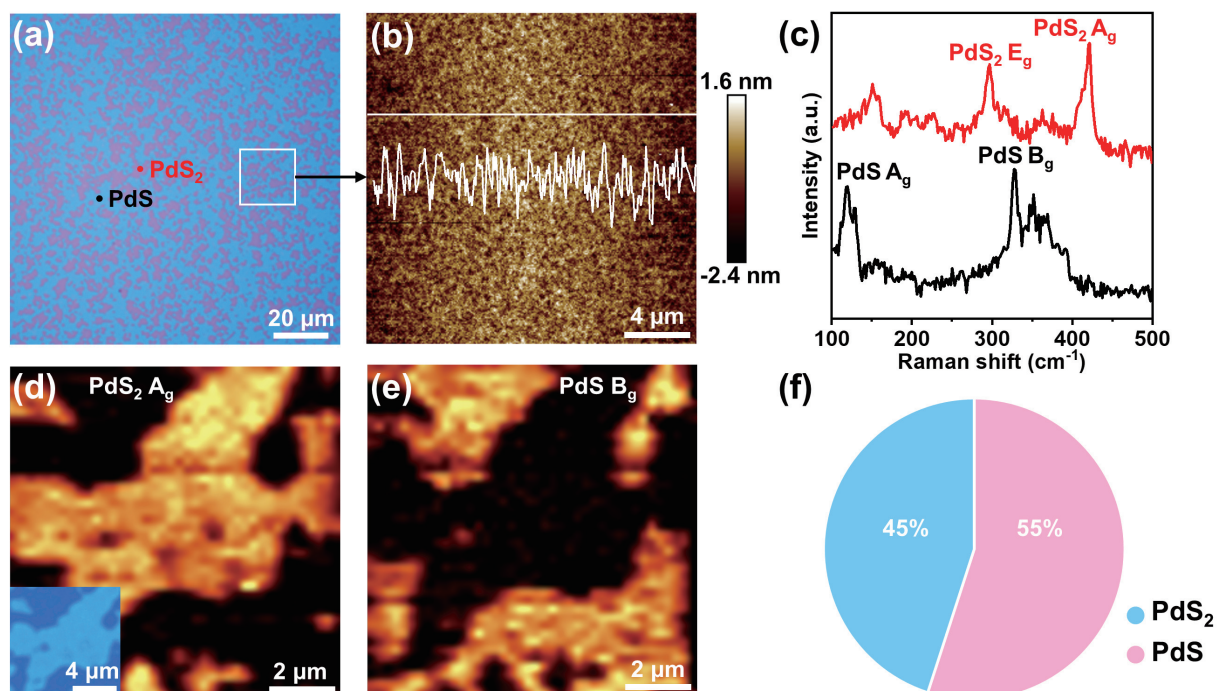
Fig. 3. (Color online) (a) OM image of PdS–PdS$_2$ hybrid NF (the thickness of pre-deposited Pd ~2 nm). (b) Corresponding AFM image. (c) Raman spectra taken from the red and black points marked in (a) corresponding to the PdS$_2$ and PdS, respectively. (d) Raman intensity mapping (A$_g$ mode) of PdS$_2$ NF. Inset: corresponding OM image. (e) Raman intensity mapping (B$_g$ mode) of PdS NF. (f) Statistical diagram of area ratio of PdS$_2$ and PdS.

cessfully fabricated just using short growth time (10 min). We have further investigated the effects of different growth temperatures on PdS$_2$ NF. Figs. S4(a)–S4 (h) show corresponding OM images under different growth temperature. It can be clearly seen that the surface of the synthesized film is very uniform. Corresponding Raman spectra indicate that PdS$_2$ cannot be synthesized under growth temperatures below 360 °C, and crystalline PdS$_2$ NFs can be successfully prepared from 400 to 650 °C (Fig. S4(i)). Furthermore, the PdS$_2$ pattern can be fabricated by sulfurizing the Pd pattern fabricated using Cu grid as physical mask, which is critical to the construction of functional devices. Fig. S5 display the OM images of the as-prepared Pd pattern before and after sulfurization. Meanwhile, uniform PdS$_2$ NF can also be prepared on soda-lime glass and *c*-plane sapphire substrates as shown in Figs. S6(a)–S6(d). The insets are the corresponding Raman spectrum. Monolayer MoS$_2$ and WS$_2$ nanoplates were also chosen as growth substrates to fabricate van der Waals (vdW) heterojunctions. Figs. S6(e) and S6(g) show the corresponding OM images of as-prepared samples. The Raman spectra further demonstrated the synthesis of PdS$_2$–WS$_2$ and PdS$_2$–MoS$_2$ heterojunctions as displayed in Figs. S6(f) and S6(h), respectively. These results reveal that our method is universal for the controllable growth of other vdW heterostructures.

Interestingly, when the thickness of pre-deposited Pd film was increased to 2 nm, the obtained sample exhibits obvious phase separation (as shown in Fig. 3(a)). Corresponding AFM image of the synthesized film reveals negligible height difference across the interface (Fig. 3(b)). Fig. 3(c) shows the Raman spectra collected from the different regions, which confirms that the separate domains are PdS$_2$ and PdS, respectively. The Raman mappings of the PdS$_2$ A$_g$ (422 cm^{-1}) peak intensity and PdS B$_g$ (327 cm^{-1}) peak intensity were col-

lected as displayed in Figs. 3(d) and 3(e), respectively. PdS$_2$ and PdS domains can be clearly distinguished with sharp interface. According to statistics in Fig. 3(f), the area proportion of PdS$_2$ is about 45% and the area proportion of PdS is about 55%. The effect of sulfurization temperature on the synthesized samples was further systematically investigated. We found that PdS$_2$–PdS hybrid NF cannot be synthesized when the sulfurization temperature was below 360 °C (Fig. S7(a)), which was confirmed by Raman spectrum as shown in Fig. S7(b). Fig. S7(c) displays the representative AFM image of as-prepared NF with the thickness ~5.91 nm. The OM image and corresponding Raman spectra of PdS$_2$-PdS hybrid NF were presented in Figs. S7(d)–S7(e) when the growth temperature is 540 °C. AFM image indicates that the thickness of as-prepared sample is 6.02 nm (Fig. S7(f)). Interestingly, pure PdS NF can be synthesized when the sulfurization temperature is up to 650 °C. Fig. S7(g) displays the OM image of as-prepared PdS NF. This is confirmed by the Raman spectrum (Fig. S7(h)). The corresponding AFM image shows that the thickness is ~6.18 nm (Fig. S7(i)). Figs. S8(a)–S8(i) show the OM images of synthesized film under different sulfurization temperatures, which demonstrate that crystalline PdS$_2$–PdS hybrid NF can be synthesized in the temperature range of 380–620 °C. Our experiments confirm that sulfurization temperature plays a crucial role for the controllable of pure PdS and PdS$_2$–PdS hybrid NFs.

When the thickness of pre-deposited Pd film was further increased to 4 nm, the as-prepared sample is still PdS$_2$–PdS hybrid NF and Fig. S9(a) shows the OM image. Fig. S9(b) is the corresponding AFM image of the PdS$_2$–PdS hybrid NF. A corresponding KFPM image is provided with sharp interface between PdS and PdS$_2$ (Fig. S9(c)). The surface potential of PdS$_2$ is determined to be 10 mV lower than PdS (Fig. S9(d)). Fig. S9(e) shows the Raman spectra of the hybrid PdS$_2$–PdS
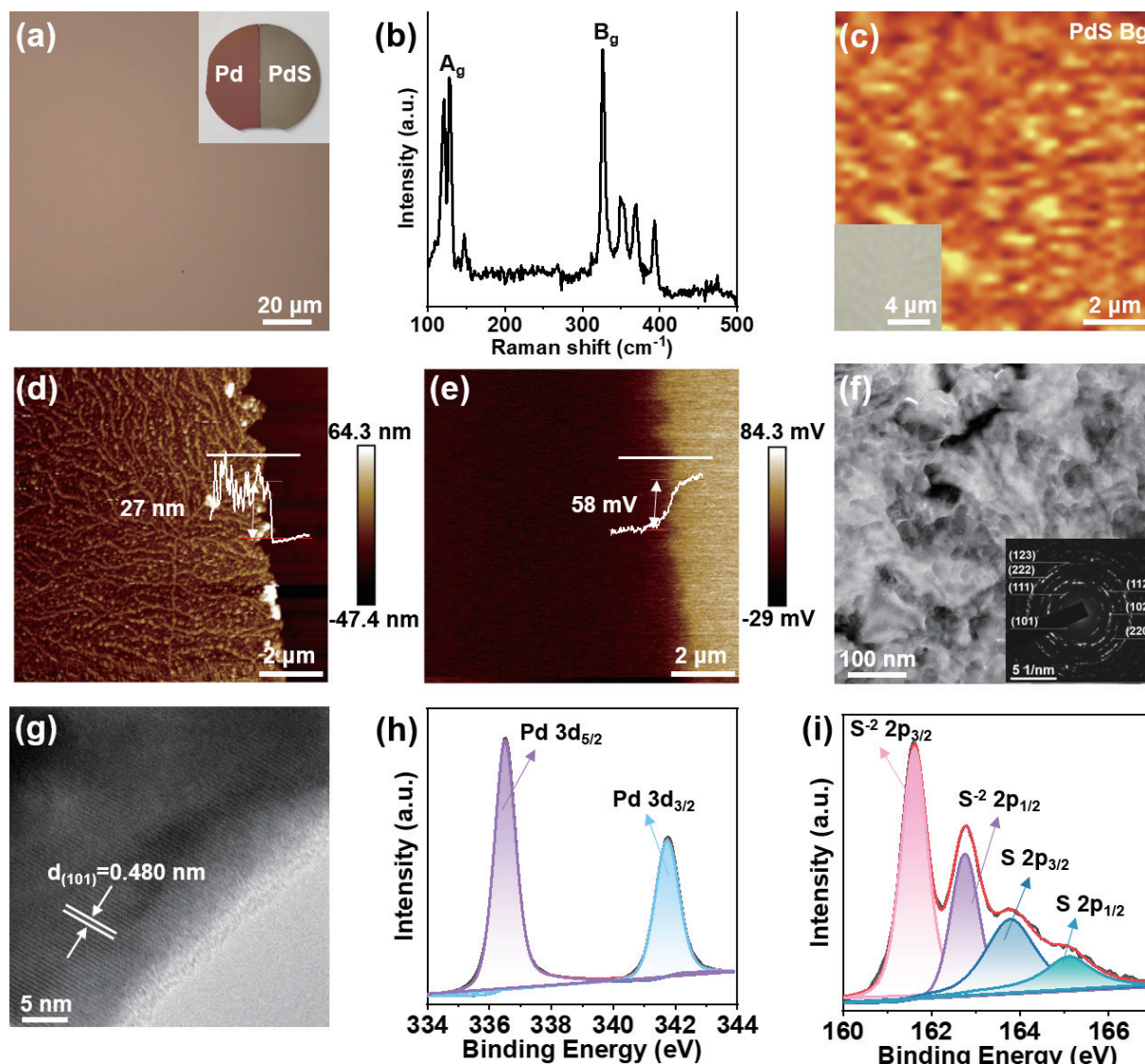
Fig. 4. (Color online) (a) OM image of as-grown PdS NF (the thickness of pre-deposited Pd ~10 nm). (b) Raman spectrum of as-prepared PdS NF. (c) Raman intensity mapping (B_g mode) of PdS NF. Inset: corresponding OM image. (d) AFM image of PdS NF. (e) Corresponding surface potential image. (f) Low-magnification TEM image of PdS NF. Inset: corresponding SAED pattern. (g) HRTEM image of the PdS NF. (h, i) XPS spectra of the PdS_2 NF corresponding to Pd $3d$ and S $2p$ core level peaks, respectively.

NF obtained from the black and red points marked in Fig. S9(a). The black line represents the PdS_2, and the red line corresponds to the PdS. Raman mappings of the representative PdS_2 Ag mode (422 cm^{-1}) and PdS B_g mode (327 cm^{-1}) are shown in Figs. S9(f) and S9(g). The inset of Fig. S9(f) corresponds to OM image. The statistical results indicate that the area proportion of PdS_2 is 5% and the area of PdS proportion is 95% (Fig. S9(h)), which indicates that the synthesis of PdS NF is preferred with increasing the thickness of pre-deposited Pd film.

Interestingly, pure PdS NF can be synthesized when the thickness of the pre-deposited Pd film finally increases to 10 nm. The OM image of PdS NF is displayed in Fig. 4(a), and the inset exhibits the corresponding photo image of 10 nm Pd film deposited on SiO₂/Si substrate and as-prepared PdS NF. Fig. 4(b) presents the typical Raman spectrum of as-prepared PdS NF. It is clearly that two vibrational Raman modes were observed, which were assigned as A_g (134 cm^{-1}), and B_g (327 cm^{-1}), respectively[30, 31]. Raman mapping (B_g mode) further demonstrates the uniformity of as-prepared PdS NF as

shown in Fig. 4(c). The thickness of PdS NF was determined to be ~27 nm investigated by AFM (Fig. 4(d)). Moreover, KPFM was carried out to detect the surface potential of synthesized PdS NF in the ambient environment, and the surface potential value of PdS is 58 mV higher than the SiO₂/Si substrate as shown in Fig. 4(e). The KPFM image of PdS NF is relatively homogeneous revealing the uniform surface potential and charge distributions. The crystallographic structure and chemical composition of PdS NF were further explored by TEM, HRTEM, SAED, and EDS characterizations. Fig. 4(f) shows a low-magnification TEM image of the as-prepared PdS NF. The inset is the corresponding SAED pattern, which suggests that the sample has a polycrystalline structure. The HRTEM image shows the corresponding atomic structure with a lattice spacing of 0.48 nm, which is consistent with (101) planes (Fig. 4(g)). The elemental compositional analysis of obtained PdS NF was performed by EDS (Fig. S10). The atomic ratio between S and Pd elements is determined to be 0.95 : 1, which is in good agreement with the stoichiometric ratio of PdS.
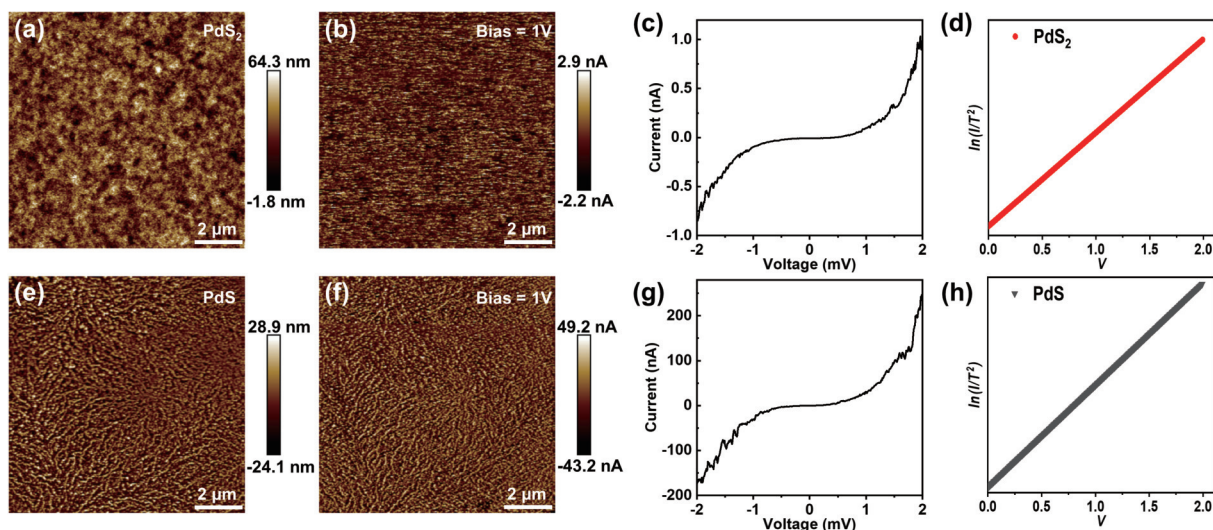
Fig. 5. (Color online) (a) AFM image of the PdS$_2$ NF grown on the SiO$_2$/Si substrate. (b) Corresponding electrical current image of the PdS$_2$ NF. (c) I–V curve of PdS$_2$ NF. (d) ln(I/T^2) verse V curve of PdS$_2$ NF fitted by the thermonic emission model. (e) AFM image of the PdS NF. (f) Corresponding electrical current image of the PdS NF. (g) I–V curve of the PdS NF. (h) ln(I/T^2) verse V curve of PdS NF fitted by the thermonic emission model.

The elemental composition and the chemical states were further characterized by XPS. The Pd 3d and S 2p core level peaks of the film are shown in Figs. 4(h) and 4(i), respectively. The palladium 3d$_{5/2}$ and 3d$_{3/2}$ peaks for PdS are determined at 336.50 eV and 341.72 eV, respectively (Fig. 4(h)). A splitting of 5.22 eV is observed for Pd-3d signal in PdS NF, which is attributed to the spin orbit coupling. As for the S 2p core level spectra, the two peaks at 164.01 and 165.21 eV are ascribed to the S 3p$_{3/2}$ and S 3p$_{1/2}$ core level spectra of the S–Pd bonding of PdS (Fig. 4(i)). It is noteworthy that the binding energy (BE) position of Pd in the PdS and PdS$_2$ samples was shifted by nearly 1.7 eV relative to pure Pd (3d$_{5/2}$ 335.1 eV) toward the high BE side. While the BE of S is shifted toward the low BE side indicating the direction of charge transfer from Pd to S, which further confirms the formation of PdS. AFM images of as-prepared samples under different sulfurization times (5, 30, 60, 90, 120, and 180 min) were performed, and the results indicate that the thicknesses of as-synthesized PdS NF were all around 30 nm after sulfurization as shown in Figs. S11(a)–S11(e). Systematic studies demonstrate that the Pd film can be completely sulfurized even under growth time as short as 5 min.

In order to reveal the corresponding growth mechanism, we have conducted thermodynamic growth investigation[32]. Once the sulfur vapor is available, the possible reactions that may initiate the sulfurization process are described by Eqs. (1)–(3):

$$Pd + S_2 \rightarrow PdS_2, \tag{1}$$

$$Pd + \frac{1}{2}S_2 \rightarrow PdS, \tag{2}$$

$$2Pd + S_2 \rightarrow 2PdS. \tag{3}$$
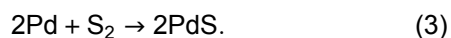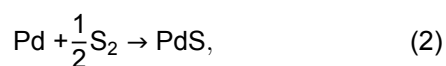
The priority of different products using the same reactants can be judged from Gibbs energy (ΔG). The ΔG of these reactions will be expressed per mole of Pd because it is the limiting reactant for the global process. Since the formation energy difference between PdS$_2$ and PdS is very small and it is hardly possible to discriminate their reaction activation energies. The evolution of the Gibbs free energy for PdS$_2$ and PdS was investigated to forecast the priorities of the reactions (1–3) at different temperatures. The detailed calculation of the Gibbs free energy is provided in the supporting information.

The dependence of ΔG_m^0 on temperature for each reaction is plotted in Fig. S12. Pd film with the thickness ~1 nm corresponds to small amount of Pd. ΔG_m^0 of Eq. (2) is lower and the reaction is more likely to occur from 600 to 900 K, so the product after sulfurization is pure PdS$_2$ NF. When the pre-deposited Pd film was 2 nm, the amount of Pd increased slightly, so the Eqs. (1) and (2) were carried out simultaneously from 600 to 900 K. The product was a PdS and PdS$_2$ hybrid NF with the PdS proportion of ~45%. When the sulfurization temperature was above 900 K, ΔG_m^0 of Eq. (1) was higher, so it was easier to synthesize PdS$_2$. More Pd can be supplied with the thickness of Pd film increased to 4 nm, therefore Eq. (3) can also take place, and the final product is in-plane PdS and PdS$_2$ hybrid NF with the proportion of PdS up to ~95%. When thickness of Pd increased to 10 nm, the supply of Pd is always sufficient for reaction. Only Eq. (3) can be carried out, which results in the synthesis of pure PdS NF.

C-AFM is an essential tool for probing local electrical conductivity and surface electrical properties of micro-nano semiconductor materials with nanometer resolution. In this study, we employ C-AFM to systematically investigate the current distribution and transport properties of PdS$_2$ and PdS NFs. Ag electrodes were made to investigate the lateral electrical measurements on the PdS$_2$ and PdS NFs. A schematic diagram of the C-AFM electrical measurement is shown in Fig. S13. Fig. 5(a) displays the AFM image of as-synthesized PdS$_2$ NF. The corresponding electrical current image of the PdS$_2$ NF was obtained under a constant bias of 1 V as shown in Fig. 5(b). The conductivity remains constant indicating uniformity of the PdS$_2$ NF. Fig. 5(c) displays the I–V curve of PdS$_2$ under the bias ranging from −2.0 to 2.0 V. The AFM image of PdS NF is shown in Fig. 5(e). Fig. 5(f) exhibits the correspond-

ing current image, which shows the uniformity of the current distribution. Fig. 5(g) shows I–V curves of PdS under the bias ranging from −2.0 to 2.0 V. The typical I–V curves obtained from the measurements exhibit obvious nonlinearity and asymmetry properties, which indicates that the Ag electrode and Pt/Ir-coated tip make two Schottky barrier (SB) contacts with the PdS or PdS_2 NFs, respectively. The back-to-back SBs are formed. Eqs. (4) and (5) are used to fit the curve and $\ln(I/T^2)$ verse V presented linear, which coincides with the transport characteristics in the thermal emission model[33, 34], as shown in Figs. 5(d)–5(h).

$$I = I_0 \left[\exp\left(\frac{qV}{\eta k_B T} \right) - 1 \right], \tag{4}$$

$$I_0 = AA^*T^2 \exp\left(-\frac{q\Phi_B}{k_B T} \right), \tag{5}$$

where I_0 is the reverse saturation current, Φ_B is the Schottky barrier, η is the ideality factor, and A^* is the Richardson constant (31.6 A/(cm·K)^2 for PdS and 96 A/(cm·K)^2 for PdS_2)[7, 35]. By fitting Eq. (4) in the electrical characteristics in the forward bias of Figs. 5(d)–5(h), the ideality factor of PdS and PdS_2 were calculated as 13.3 and 14.3, respectively. Our studies could provide experimental support for the fabrication of TMDs NFs optoelectronic devices.

The electrical transport properties of as-synthesized PdS_2 NF were further investigated and PdS_2-based TFT have been fabricated. Fig. S14(a) displays the photographic images of PdS_2 TFT arrays. Fig. S14(b) is corresponding OM image of one typical TFT device. It can be clearly seen that the PdS_2 NF presents typical n-type semiconductor characteristics with an on/off ratio of about 9.2 (Figs. S14(c) and S14(d)). The field effect mobility was evaluated from the equation:

$$\mu = \frac{L}{W} \frac{dI_{ds}}{dV_{gs}} \frac{d}{\varepsilon_0 \varepsilon_r V_{ds}}, \tag{6}$$

where L = 20 μm and W = 130 μm are the channel length and width, respectively, $\varepsilon_0 = 8.85 \times 10^{12}$ F/m is the vacuum permittivity, ε_r = 3.9 is the relative dielectric constant of SiO_2, d = 300 nm is its thickness, and V_{ds} = 1 V. The field-effect mobility was determined to be about 0.017 cm^2/(V·s). Our work presents a convenient chemical route to construct high-performance n-type TFT with low-dimensional materials for future electronics.

4. Conclusion

In summary, wafer-scale PdS and PdS_2 NFs have been successfully synthesized via atmospheric pressure CVD combined with EBE technique. The uniform pre-deposited Pd film promotes the growth of wafer-scale PdS_2 NF. Our experimental results demonstrate that the thickness of pre-deposited Pd film and sulfurization temperature play important roles for the precise synthesis of pure PdS_2 and PdS NFs. The corresponding growth mechanism was further illuminated through the thermionic growth study. We have systematically investigated the electrical transport properties of PdS_2 and PdS NFs by C-AFM, which can be illuminated by thermonic emission model. These results provide a new route for the controllable synthesis of large-area nTMDs NFs, which is beneficial for their applications in high-performance electronic and optoelectronic devices.

Appendix A. Supplementary material

Supplementary materials to this article can be found online at https://doi.org/10.1088/1674-4926/44/12/122001.

References

[1] Novoselov K S, Geim A K, Morozov S V, et al. Electric field effect in atomically thin carbon films. Science, 2004, 306, 666

[2] Wang Q H, Kalantar-Zadeh K, Kis A, et al. Electronics and optoelectronics of two-dimensional transition metal dichalcogenides. Nat Nanotechnol, 2012, 7, 699

[3] Chen T, Hao G L, Wang G, et al. Controlled growth of atomically thin MoSe$_2$ films and nanoribbons by chemical vapor deposition. 2D Mater, 2019, 6, 025002

[4] Duan Z J, Chen T, Shi J W, et al. Space-confined and substrate-directed synthesis of transition-metal dichalcogenide nanostructures with tunable dimensionality. Sci Bull, 2020, 65, 1013

[5] Kempt R, Kuc A, Heine T. Two-dimensional noble-metal chalcogenides and phosphochalcogenides. Angew Chem Int Ed, 2020, 59, 9242

[6] Miró P, Ghorbani-Asl M, Heine T. Two dimensional materials beyond MoS$_2$: Noble-transition-metal dichalcogenides. Angew Chem Int Ed, 2014, 53, 3015

[7] Wang Y, Li Y F, Chen Z F. Not your familiar two dimensional transition metal disulfide: Structural and electronic properties of the PdS$_2$ monolayer. J Mater Chem C, 2015, 3, 9603

[8] Wang Y W, Zhou L, Zhong M Z, et al. Two-dimensional noble transition-metal dichalcogenides for nanophotonics and optoelectronics: Status and prospects. Nano Res, 2022, 15, 3675

[9] Song S, Sim Y, Kim S Y, et al. Wafer-scale production of patterned transition metal ditelluride layers for two-dimensional metal–semiconductor contacts at the Schottky–Mott limit. Nat Electron, 2020, 3, 207

[10] Cheng P K, Liu S X, Ahmed S, et al. Ultrafast Yb-doped fiber laser using few layers of PdS$_2$ saturable absorber. Nanomaterials, 2020, 10, 2441

[11] Cheng P K, Tang C Y, Wang X Y, et al. Passively Q-switched and femtosecond mode-locked erbium-doped fiber laser based on a 2D palladium disulfide (PdS$_2$) saturable absorber. Photon Res, 2020, 8, 511

[12] Ghorbani-Asl M, Kuc A, Miró P, et al. A single-material logical junction based on 2D crystal PdS$_2$. Adv Mater, 2016, 28, 853

[13] Zhang X D, Su G W, Lu J W, et al. Centimeter-scale few-layer PdS$_2$: Fabrication and physical properties. ACS Appl Mater Interfaces, 2021, 13, 43063

[14] He K, Xu W T, Tang J M, et al. Centimeter-scale PdS$_2$ ultrathin films with high mobility and broadband photoresponse. Small, 2023, 19, 2206915

[15] Lan Y S, Chen X R, Hu C E, et al. Penta-PdX$_2$ (X = S, Se, Te) monolayers: Promising anisotropic thermoelectric materials. J Mater Chem A, 2019, 7, 11134

[16] Figueiredo R O, Seixas L. Hydrogen-evolution reaction in two-dimensional PdS$_2$ by phase and defect engineering. Phys Rev Applied, 2022, 17, 034035

[17] Guha A K, Sharma R, Sahoo K R, et al. One-dimensional hollow structures of 2O-PdS$_2$ decorated carbon for water electrolysis. ACS Appl Energy Mater, 2021, 4, 8715

[18] ElGhazali M A, Naumov P G, Mu Q, et al. Pressure-induced metallization, transition to the pyrite-type structure, and superconductivity in palladium disulfide PdS$_2$. Phys Rev B, 2019, 100, 014507

[19] Zheng J Y, Miao T T, Xu R, et al. Chemical synthesis and integration of Highly conductive PdTe$_2$ with low-dimensional semiconductors for p-type transistors with low contact barriers. Adv Mater, 2021, 33, 2101150

[20] Wang Y H, Zhang Y H, Cheng Q L, et al. Large area uniform PtS$_x$ synthesis on sapphire substrate for performance improved photodetectors. Appl Mater Today, 2021, 25, 101176

[21] Zhang K N, Wang M, Zhou X, et al. Growth of large scale PtTe, PtTe$_2$ and PtSe$_2$ films on a wide range of substrates. Nano Res, 2021, 14, 1663

[22] Ferrer I J, Díaz-Chao P, Pascual A, et al. An investigation on palladium sulphide (PdS) thin films as a photovoltaic material. Thin Solid Films, 2007, 515, 5783

[23] Barawi M, Ferrer I J, Ares J R, et al. Hydrogen evolution using palladium sulfide (PdS) nanocorals as photoanodes in aqueous solution. ACS Appl Mater Interfaces, 2014, 6, 20544

[24] Chen L C, Jiang B B, Yu H, et al. Thermoelectric properties of polycrystalline palladium sulfide. RSC Adv, 2018, 8, 13154

[25] Folmer J C W, Turner J A, Parkinson B A. Photoelectrochemical characterization of several semiconducting compounds of palladium with sulfur and/or phosphorus. J Solid State Chem, 1987, 68, 28

[26] Sun G T, Mao S M, Ma D D, et al. One-step vulcanization of Cd(OH)Cl nanorods to synthesize CdS/ZnS/PdS nanotubes for highly efficient photocatalytic hydrogen evolution. J Mater Chem A, 2019, 7, 15278

[27] Li Y, Yu S, Xiang J L, et al. Revealing the importance of hole transfer: Boosting photocatalytic hydrogen evolution by delicate modulation of photogenerated holes. ACS Catal, 2023, 13, 8281

[28] Bhatt R, Bhattacharya S, Basu R, et al. Growth of Pd$_4$S, PdS and PdS$_2$ films by controlled sulfurization of sputtered Pd on native oxide of Si. Thin Solid Films, 2013, 539, 41

[29] Zhao D H, Xie S, Wang Y, et al. Synthesis of large-scale few-layer PtS2 films by chemical vapor deposition. AIP Adv, 2019, 9, 025225

[30] Chen L C, Cao Z Y, Yu H, et al. Phonon anharmonicity in thermoelectric palladium sulfide by Raman spectroscopy. Appl Phys Lett, 2018, 113, 022105

[31] Chen L C, Peng Q, Yu H, et al. Lattice dynamics of thermoelectric palladium sulfide. J Alloys Compd, 2019, 798, 484

[32] Diaz-Chao P, Ferrer I J, Ares J R, et al. Cubic Pd$_{16}$S$_7$ as a precursor phase in the formation of tetragonal PdS by sulfuration of Pd thin films. J Phys Chem C, 2009, 113, 5329

[33] Li Y, Xu C Y, Zhen L. Surface potential and interlayer screening effects of few-layer MoS$_2$ nanoflakes. Appl Phys Lett, 2013, 102, 143110

[34] Khan A R, Lu T, Ma W D, et al. Tunable optoelectronic properties of WS$_2$ by local strain engineering and folding. Adv Electron Mater, 2020, 6, 1901381

[35] Ali S M, AlGarawi M S, Khan S U D, et al. Nanostructure, optical and electrical response of gamma ray radiated PdS/p-Si heterojunction. Mater Sci Semicond Process, 2021, 122, 105474

Hui Gao graduated from North University of China with a B.S degree in 2020. She is currently a M.S student under the supervision of Prof. Guolin Hao at Xiangtan University. Her research mainly focuses on controllable synthesis of controllable synthesis of 2D materials.

Hongyi Zhou is now an undergraduate majoring in optoelectronics information science and engineering of Xiangtan University. Her research mainly focuses on controllable synthesis of transition-metal dichalcogenide nanostructures by CVD method.

Yulong Hao graduated from Shandong Normal University Lishan College with a B.S degree in 2021. Now he is a M.S student at Guangxi Normal University. His research interests focus on carbon-based micro and nano devices and advanced sensors.

Guolin Hao received his B.S. degree in Physics from Shandong Normal University in 2008, and his Ph.D. degree in Physics from Xiangtan University in 2013. He worked as a postdoctoral researcher at University of California, Los Angeles during 2015–2017. He is currently a professor in School of Physics and Optoelectronics at Xiangtan University. His research is mainly focused on synthesis and application of 2D materials.